

Supporting Information

Predicting calcification risk in prosthetic aortic valves: a hybrid physics-based and machine learning approach

Pascal Corso¹, Giorgia Tagliavini², Maria Giuseppina Chiara Nestola³, Fergal Brian Coulter⁴

Correspondence: Pascal Corso, ETH Zurich, Switzerland.

E-mail: `pascal.corso@sdsc.ethz.ch`

This document provides supplementary material to the main manuscript. Video V1 shows the leaflet motion throughout systole for all six valve configurations. Fig. S1 reports the silhouette analysis justifying the choice of $K = 4$ clusters for the k -means classification. Fig. S2 presents the temporal evolution of the spatially maximum and averaged WSS magnitude throughout systole. Figs S3 and S4 present the spatial distributions of the temporal features extracted from the FTLE and WSS fields fed into the k -means classification, together with their interpretation. Fig. S5 presents, for each valve configuration, the high-risk surface fraction and the proportion of leaflet surface nodes assigned to each risk category for both the FTLE- and WSS-based classifications.

Selection of the optimal number of clusters K

The silhouette score measures the compactness and separation of the clusters produced by the k -means algorithm. For a given partition into K clusters, the score at node i is $(b_i - a_i) / \max(a_i, b_i)$, where a_i is the mean intra-cluster distance to all other nodes in the same cluster and b_i the mean distance to nodes in the nearest neighbouring cluster; the

overall score is the mean over all nodes. Values close to 1 indicate well-separated, compact clusters; values near 0 signal overlap between neighbouring clusters.

Figure S1 presents the silhouette scores as a function of $K \in \{2, \dots, 8\}$ for both the WSS-based and FTLE-based analyses. In both cases the score peaks unambiguously at $K = 4$ (WSS-based: 0.481; FTLE-based: 0.482), with a pronounced drop for $K \geq 5$. Four clusters are therefore adopted throughout.

[Figure 1 about here.]

Temporal evolution of WSS magnitude throughout systole

Figure S2 presents the time evolution of the spatially maximum (panels A, B) and spatially averaged (panels C, D) WSS magnitude $\|\mathbf{WSS}\|$ on the ventricular side of the leaflets for the D1^V (panels A, C) and D2^U (panels B, D) geometries. For D1^V, D1^V-ELA and D1^V-BOV attain the highest spatially averaged WSS during peak systole (≈ 3.0 and ≈ 2.75 Pa respectively; Fig. S2C), whilst D1^V-PORC remains systematically lower (below ≈ 2.5 Pa) owing to its wider orifice, which distributes the systolic jet over a broader cross-section. The maximum WSS signals for D1^V (Fig. S2A) are broadly comparable across materials (≈ 10 -20 Pa) and display the temporal irregularity associated with leaflet flapping in the BOV and PORC cases. For D2^U, D2^U-ELA sustains the highest spatially averaged WSS throughout most of systole (≈ 2.7 Pa at peak; Fig. S2D), consistent with the sustained 45-60 Hz flutter documented in Section 3.1 of the main manuscript. D2^U-BOV remains the lowest of all six configurations (≈ 1.35 Pa; Fig. S2D). D2^U-PORC exhibits pronounced instantaneous WSS peaks (≈ 25 -30 Pa; Fig. S2B) driven by 45 Hz leaflet flapping, whilst the spatially averaged value remains moderate (≈ 1.5 Pa; Fig. S2D).

[Figure 2 about here.]

Temporal features of the FTLE and WSS fields

The spatial distributions of the temporal minimum of the FTLE and the temporal standard deviation of $\|\mathbf{WSS}\|$ on the three leaflets (L1, L2, L3) are presented for all six valve configurations in Figs S3 and S4, respectively. The FTLE field is computed on the aortic side whereas the WSS field is evaluated on the ventricular side of the leaflets. In both figures (Figs. S3A and S4A), configurations are arranged from top to bottom in ascending order of the corresponding overall risk score RS (Section 3.6 of the main manuscript). Each figure includes a scatter plot (Figs S3B and S4B) condensing the leaflet-surface data into a single point per configuration.

The temporal-minimum FTLE fields (Fig. S3A) delineate the zones that, throughout systole, sustain the highest rates of material point separation. Across all configurations elevated FTLE values are concentrated in the central and lower belly, extending towards the commissures. D2^U-BOV presents the lowest values overall: surfaces remain uniformly dark (temporal-minimum FTLE < 400) and the scatter plot (Fig. S3B) places this configuration in the low-FTLE corner (spatially averaged temporal-minimum FTLE ≈ 300 , spatially averaged temporal-maximum FTLE $\approx 6,100$). D1^V-ELA and D2^U-ELA display moderate and spatially heterogeneous patterns, forming a tight cluster in the scatter plot in Fig. S3B (temporal-minimum FTLE ≈ 400 -500, temporal-maximum FTLE $\approx 6,000$ -6,800). D1^V-BOV produces intermediate FTLE levels concentrated in the belly (temporal-minimum FTLE ≈ 800 , temporal-maximum FTLE $\approx 7,000$). The two porcine configurations stand apart: D1^V-PORC and D2^U-PORC exhibit temporal-minimum FTLE values exceeding 1,000 over large portions of the belly, with D2^U-PORC reaching the most extreme levels (spatially averaged temporal-minimum FTLE $\approx 1,200$, temporal-maximum FTLE $> 10,000$). In D2^U-PORC, the elevated region spans nearly the entire belly surface on all three leaflets (see Fig. S3A). This behaviour originates from the pronounced anisotropy of porcine tissue, whose strong circumferential-to-axial stiffness contrast produces heterogeneous strain fields with steep spatial gradients across the belly, raising both the temporal-minimum FTLE and its local spatial variations. A positive correlation between the spatially averaged temporal-

minimum and temporal-maximum FTLE is apparent in the scatter plot (Fig. S3B). This means that configurations sustaining elevated baseline deformation rates throughout systole also attain the highest instantaneous peak FTLE values.

The temporal standard deviation of $\|\mathbf{WSS}\|$ (Fig. S4A) identifies the zones of the leaflets subject to the most oscillatory shear loading over systole. Higher values (approaching 2 Pa) concentrate in the belly and near the free edge, where the proximity of the high-velocity jet and periodic flow separation generate substantial shear fluctuations. D2^U-BOV presents the lowest temporal WSS variability. In fact, surfaces are uniformly dark and the scatter plot (Fig. S4B) places this configuration in the low-variability, low-mean-WSS corner (spatially averaged temporal standard deviation ≈ 0.8 Pa, spatially averaged TAWSS ≈ 1.35 Pa). D2^U-PORC and D1^V-PORC occupy a close intermediate region in the scatter plot (Fig. S4B), with comparable temporal standard deviations (≈ 1.05 -1.1 Pa) but differing TAWSS (≈ 1.5 and ≈ 1.7 Pa, respectively). The wide porcine orifice distributes the systolic jet and entails moderate mean shear, yet the 45 Hz flapping (Section 3.1 of the main manuscript) sustains WSS fluctuations well above those of the quiescent D2^U-BOV. D1^V-BOV and D1^V-ELA cluster at higher TAWSS (≈ 1.95 -2.0 Pa) and intermediate temporal standard deviations (≈ 1.2 -1.25 Pa). Their narrower orifice areas produce a faster, more concentrated jet that raises mean shear across the ventricular leaflet surface (Fig. 5 of the main manuscript). D2^U-ELA presents the highest spatially averaged temporal standard deviation (≈ 1.4 Pa) with a TAWSS of ≈ 1.83 Pa, consistent with the sustained 45-60 Hz flutter documented in Section 3.1 and Table 3 of the main manuscript.

The ordering of configurations by ascending WSS-based risk score (D2^U-BOV, D2^U-PORC, D1^V-PORC, D1^V-ELA, D1^V-BOV, D2^U-ELA) diverges from the FTLE-based ordering (D2^U-BOV, D1^V-ELA, D2^U-ELA, D1^V-BOV, D1^V-PORC, D2^U-PORC). This divergence underscores the complementary nature of the two descriptors. Indeed, the FTLE field quantifies the rate of structural material point separation on the leaflet surface whereas the WSS field captures the haemodynamic shear environment at the ventricular surface.

[Figure 3 about here.]

[Figure 4 about here.]

High-risk surface fractions and cluster compositions

Figure S5 presents the high-risk surface fractions and the distribution of leaflet mesh nodes across the four risk categories for the FTLE-based (panels A, B) and WSS-based (panels C, D) analyses. For the FTLE-based analysis, the high-risk fraction spans from 0.9% (D2^U-BOV) to 30.9% (D2^U-PORC), with the two porcine configurations separated from the remaining four by a wide margin (Fig. 5A, B). For the WSS-based analysis, D2^U-BOV again records the lowest high-risk fraction (6.4%) whilst D2^U-ELA reaches the highest (45.5%, Fig. 5C, D). Notably, the overall RS^{WSS} of D1^V-BOV (50.2%, Fig. 9B of the main manuscript) exceeds that of D1^V-ELA (48.0%) despite its lower high-risk fraction (34.9% versus 38.7%, Fig. 5C), owing to a broader contribution from medium-high risk nodes in the composite score (Eq. 13 of the main manuscript).

[Figure 5 about here.]

Supplementary video

Video V1. Leaflet motion throughout systole for all six valve configurations (D1^V-ELA, D1^V-BOV, D1^V-PORC, D2^U-ELA, D2^U-BOV and D2^U-PORC). Each frame shows the deformed leaflet and crown volumes relative to the initial position at $t = 0$ s, viewed in perspective from above the aortic side. Playback covers the full systolic interval (0-0.25 s) repeated twice.

List of Figures

S1	Silhouette score as a function of the number of clusters K for the WSS-based (left, blue) and FTLE-based (right, red) k -means classifications. The optimal value $K = 4$ (silhouette scores 0.481 and 0.482 respectively) is highlighted.	7
S2	Time evolution of the spatially maximum (panels A , B) and spatially averaged (panels C , D) WSS magnitude $\ \mathbf{WSS}\ $ [Pa] on the ventricular side of the leaflets throughout systole for the D1 ^V (panels A , C) and D2 ^U (panels B , D) geometries.	8
S3	FTLE-based features for the k -means classification. (A) Spatial distribution of the temporal minimum of the FTLE on the aortic surface of the three leaflets (L1, L2, L3) for all six valve configurations. Colour scale: 100 (dark, low FTLE) to 2,000 (bright, high FTLE). Configurations are ordered by ascending FTLE-based calcification risk score RS . (B) Scatter plot of the spatially averaged temporal-maximum FTLE as a function of the spatially averaged temporal-minimum FTLE for each valve configuration.	9
S4	WSS-based features for the k -means classification. (A) Spatial distribution of the temporal standard deviation of $\ \mathbf{WSS}\ $ [Pa] on the ventricular surface of the three leaflets (L1, L2, L3) for all six valve configurations. Colour scale: 0 (dark) to 2 Pa (bright). Configurations are ordered by ascending WSS-based calcification risk score RS . (B) Scatter plot of the spatially averaged TAWSS as a function of the spatially averaged temporal standard deviation of $\ \mathbf{WSS}\ $ for each valve configuration.	10
S5	Calcification risk analysis for the six valve configurations. (A) FTLE-based high-risk surface fraction. (B) FTLE-based cluster composition showing the proportion of leaflet surface area in each risk category (low, medium-low, medium-high and high). (C) WSS-based high-risk surface fraction. (D) WSS-based cluster composition.	11

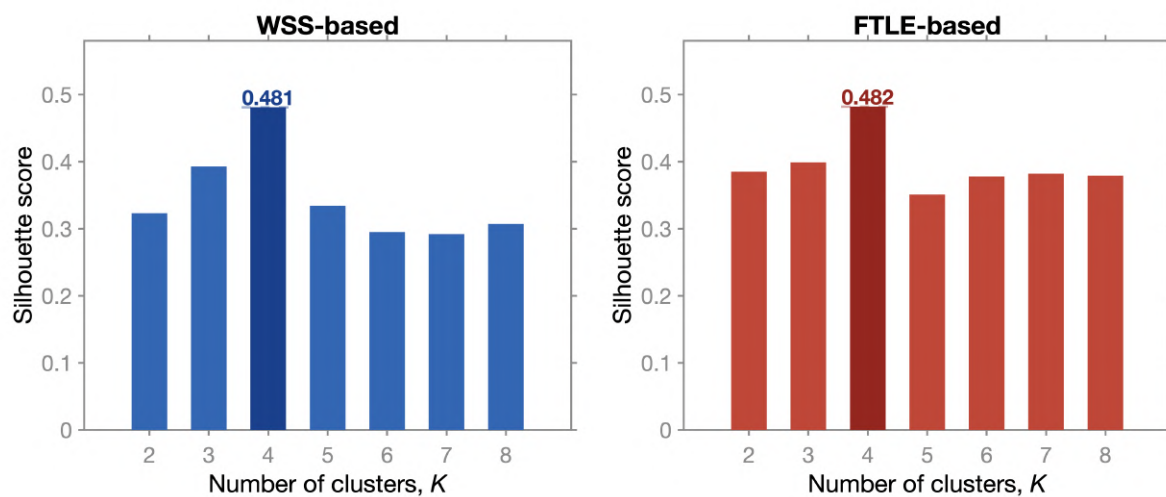


Figure S1: Silhouette score as a function of the number of clusters K for the WSS-based (left, blue) and FTLE-based (right, red) k -means classifications. The optimal value $K = 4$ (silhouette scores 0.481 and 0.482 respectively) is highlighted.

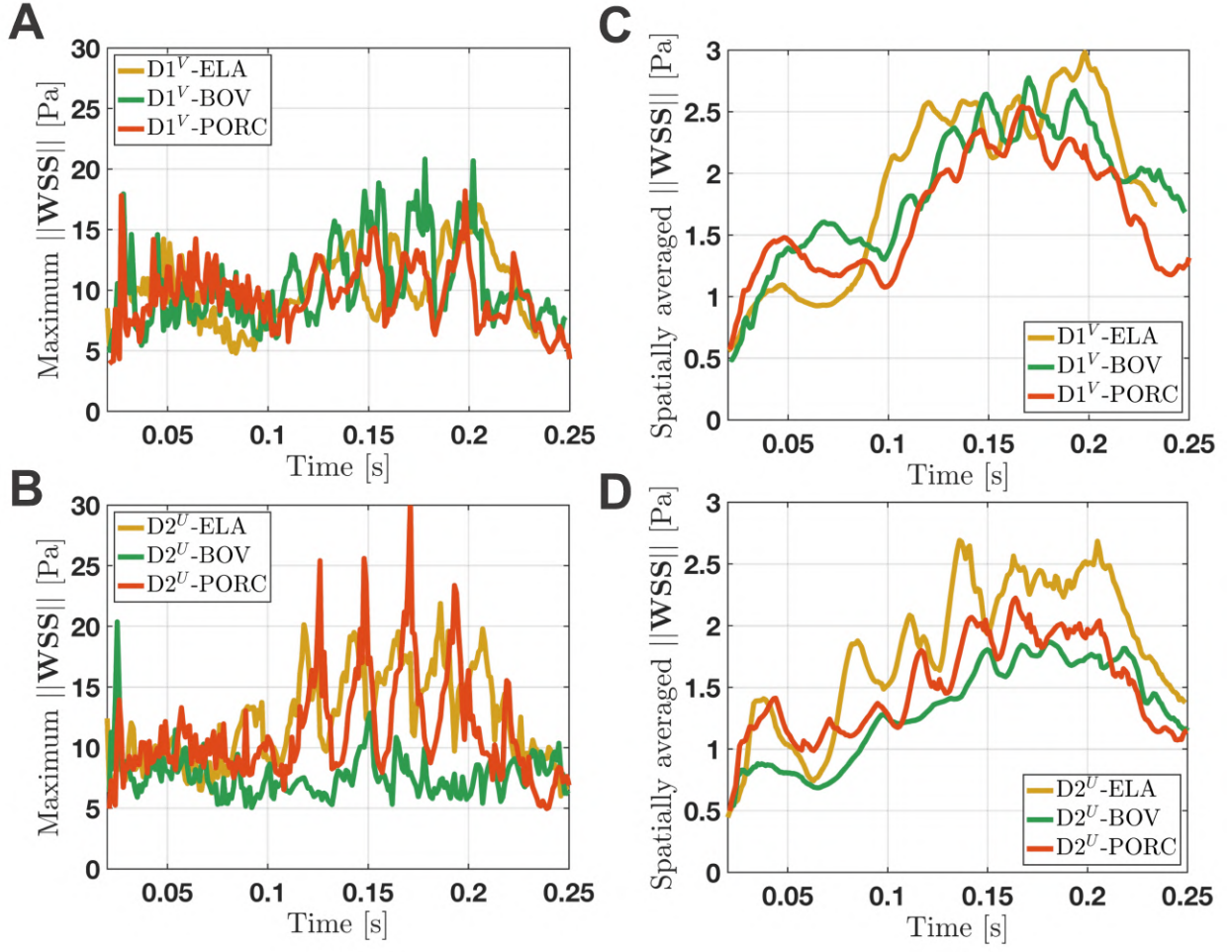


Figure S2: Time evolution of the spatially maximum (panels **A**, **B**) and spatially averaged (panels **C**, **D**) WSS magnitude $\|\mathbf{WSS}\|$ [Pa] on the ventricular side of the leaflets throughout systole for the D1^V (panels **A**, **C**) and D2^U (panels **B**, **D**) geometries.

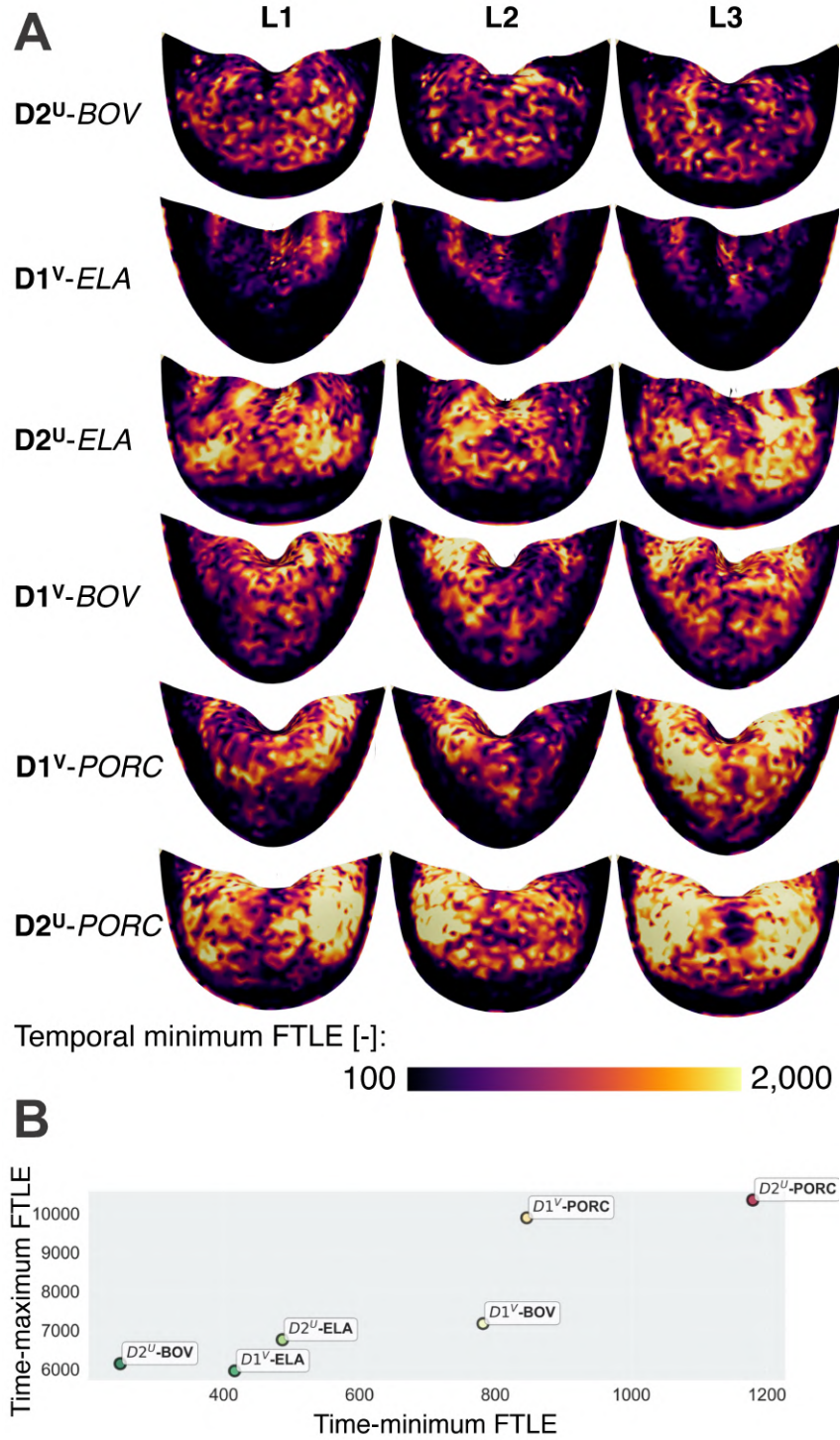


Figure S3: FTLE-based features for the k -means classification. (A) Spatial distribution of the temporal minimum of the FTLE on the aortic surface of the three leaflets (L1, L2, L3) for all six valve configurations. Colour scale: 100 (dark, low FTLE) to 2,000 (bright, high FTLE). Configurations are ordered by ascending FTLE-based calcification risk score RS . (B) Scatter plot of the spatially averaged temporal-maximum FTLE as a function of the spatially averaged temporal-minimum FTLE for each valve configuration.

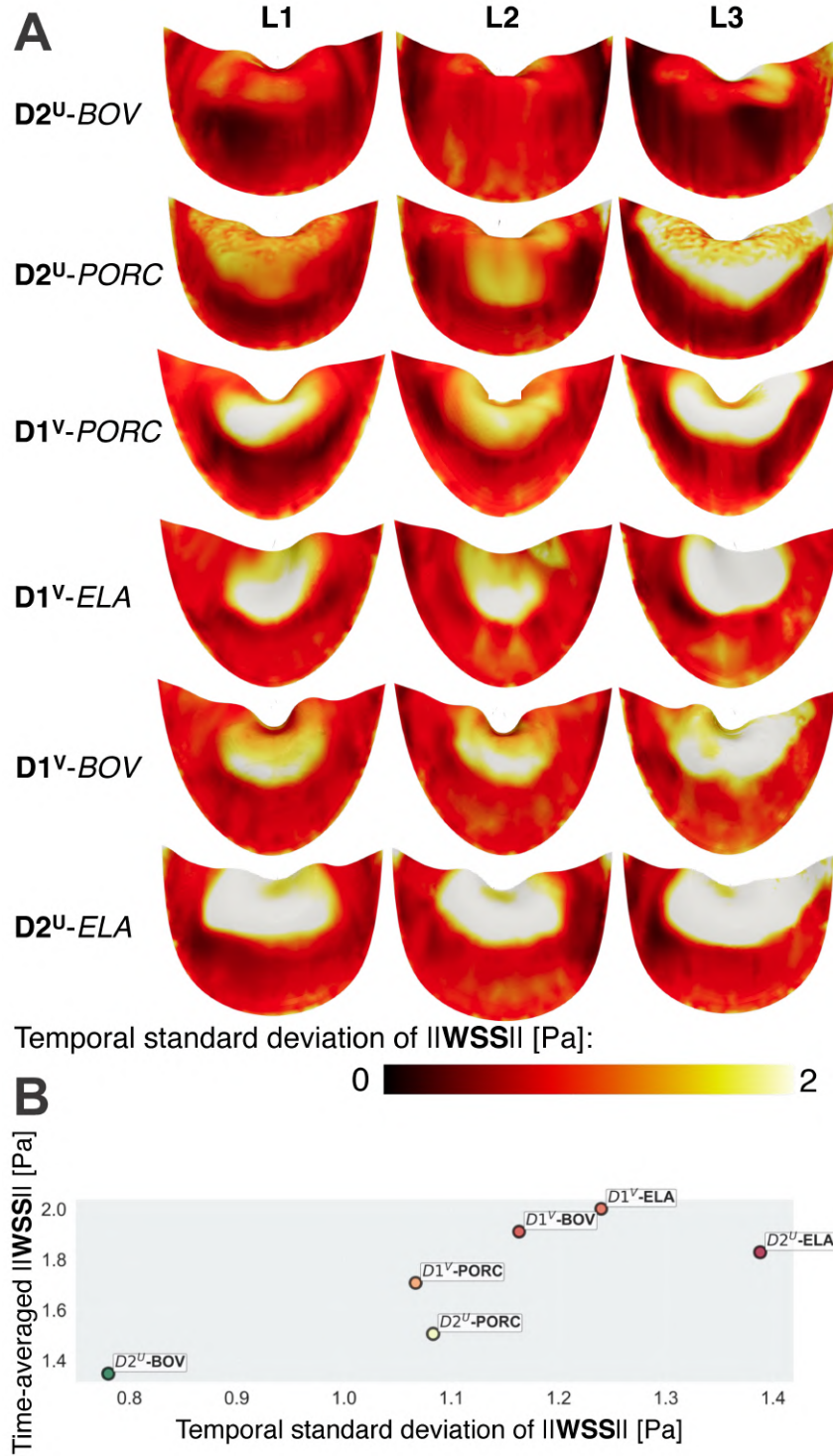


Figure S4: WSS-based features for the k -means classification. (A) Spatial distribution of the temporal standard deviation of $\|\mathbf{WSS}\|$ [Pa] on the ventricular surface of the three leaflets (L1, L2, L3) for all six valve configurations. Colour scale: 0 (dark) to 2 Pa (bright). Configurations are ordered by ascending WSS-based calcification risk score RS . (B) Scatter plot of the spatially averaged TAWSS as a function of the spatially averaged temporal standard deviation of $\|\mathbf{WSS}\|$ for each valve configuration.

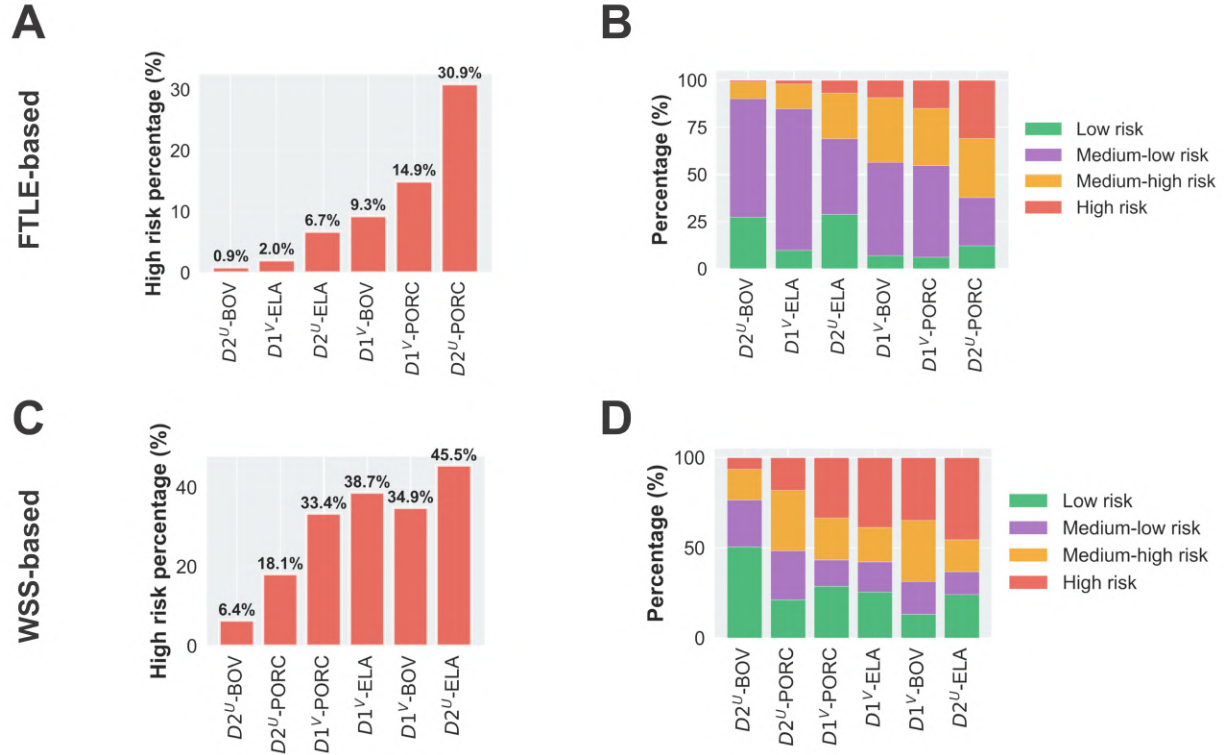


Figure S5: Calcification risk analysis for the six valve configurations. (A) FTLE-based high-risk surface fraction. (B) FTLE-based cluster composition showing the proportion of leaflet surface area in each risk category (low, medium-low, medium-high and high). (C) WSS-based high-risk surface fraction. (D) WSS-based cluster composition.